Available online at www.sciencedirect.com
ScienceDirect
Journal of Sound and Vibration 320 (2009) 859–877
JOURNAL OF SOUND AND VIBRATION
www.elsevier.com/locate/jsvi

Strong coupling strategy for fluid–structure interaction problems in supersonic regime via fixed point iteration

Mario A. Storti*, Norberto M. Nigro, Rodrigo R. Paz, Lisandro D. Dalcín

Centro Internacional de Métodos Computacionales en Ingeniería (CIMEC), INTEC(CONICET-UNL), Güemes 3450, (S3000GLN) Santa Fe, Argentina

Received 26 April 2006; received in revised form 30 June 2008; accepted 3 September 2008
Handling Editor: S. Bolton
Available online 7 November 2008

Abstract

In this paper some results on the convergence of the Gauss–Seidel iteration when solving fluid/structure interaction problems with strong coupling via fixed point iteration are presented. The flow-induced vibration of a flat plate aligned with the flow direction at supersonic Mach number is studied. The precision of different predictor schemes and the influence of the partitioned strong coupling on stability is discussed.

1. Introduction

Multidisciplinary and multiphysics coupled problems represent nowadays a paradigm when studying/analyzing even more complex phenomena that appear in nature and in new technologies. There exists a great number of problems where different physical processes (or models) converge, interacting in a strong or weak fashion (e.g. acoustics/noise disturbances in flexible structures, magneto-hydrodynamics devices, micro-electro-mechanical devices, thermo-mechanical problems like continuous casting process, fluid/structure interaction (FSI) like wing flutter problem or flow-induced pipe vibrations). In the FSI area, the dynamic interaction between an elastic structure and a compressible fluid has been the subject of intensive investigations in the last years [1–3]. This paper concerns with the numerical integration of this type of problems when they are coupled in a loose or strong manner.

For simple structural problems (like hinged rigid rods with one or two vibrational degrees of freedom) it is possible to combine into a single (simple) formulation the fluid and the structural governing equations [4]. In those cases, a fully explicit or fully implicit treatment of the coupled fluid/structure equations is attainable. Nevertheless, for complex/large scale structural problems, the simultaneous solution of the fluid and structure equations using a 'monolithic' scheme may be mathematically unmanageable or its implementation can be a

*Corresponding author.
E-mail addresses: mstorti@intec.unl.edu.ar (M.A. Storti), nnigro@intec.unl.edu.ar (N.M. Nigro), rodrigop@intec.unl.edu.ar (R.R. Paz), dalcinl@intec.unl.edu.ar (L.D. Dalcín).
URL: http://www.cimec.org.ar

0022-460X/$ - see front matter
doi:10.1016/j.jsv.2008.09.028

laborious task. Furthermore, the monolithic coupled formulation would change significantly if different fluid and/or structure models were considered.

An efficient alternative is to solve each subproblem in a partitioned procedure where time and space discretization methods could be different. Such a scheme simplifies explicit/implicit integration and it is in favor of the use of different codes specialized on each subarea. In this work a staggered fluid/structure coupling algorithm is considered. There exist various procedures how to couple the fluid and structure solvers: the coupling conditions and the moving interface can be treated in a fully explicit or implicit or in a mixed explicit/implicit manner. This approach allows a smooth transition between 'loose' and 'strong' coupling. For stability reasons, often a fully implicit formulation has to be used [5]. In this approach, we have to solve a large system of nonlinear equations with the use of the (iterative) solvers for the subsystems. Usually, this is done with Block-Jacobi, Block-Gauss–Seidel or related relaxation methods [6,7]. A detailed description of the 'state of the art' in the computational FSI area can be found in works [2,8–12] and the references therein. In this work the Gauss–Seidel iteration approach is used and its convergence is studied for high speed flows.

Beyond the physical and engineering importance, this problem is interesting from the computational point of view as a paradigm of multiphysics code implementation that reuses preexistent fluid and elastic solvers. The partitioned algorithm is implemented in the PETSc-FEM code [13] which is a parallel multiphysics finite element program based on the Message Passing Interface MPI and the Portable Extensible Toolkit for Scientific Computations PETSc. Two instances of the PETSc-FEM code simulate each subproblem and communicate interface forces and displacements via Standard C *FIFO* files or 'pipes'. The key point in the implementation of this partitioned scheme is the data exchange and synchronization between both parallel processes. These tasks are made in a small external C++ routine.

2. Strongly coupled partitioned algorithm via fixed point iteration

In this section the temporal algorithm that performs the coupling between the structure and the fluid codes is described. It is a fixed point iteration scheme over the states of both fluid and structure systems. Each iteration of the loop is called a 'stage', so if the 'stage loop' converges, then a '*strongly coupled*' algorithm is obtained. Hereafter, this algorithm is called 'staged algorithm'. The basic staggered procedure considered in this work proceeds as follows: (i) transfer the motion of the wet boundary of the solid to the fluid problem, (ii) update the position of the fluid boundary and the bulk fluid mesh accordingly, (iii) advance the fluid system and compute new pressures (and the stress field if compressible Navier–Stokes model is adopted), (iv) convert the new fluid pressure (and stress field) into a structural load, and (v) advance the structural system under the flow loads. Such a staggered procedure, which can be treated as a weakly coupled solution algorithm, can also be equipped with an outer loop in order to assure the convergence of the interaction process. The algorithm can be stated as in Table 1, where, at time t^n, we define $\mathbf{w}^n$ to be the fluid state vector $(\rho, \mathbf{v}, p)$, $\mathbf{u}^n$ to be the displacement vector (structure state vector), $\dot{\mathbf{u}}^n$ the structure velocities and $\mathbf{X}^n$ the fluid mesh node positions. n_{step} is the number of time steps in the simulation, n_{stage} the number of stages in the coupling scheme and n_{nwt} the number of Newton loops in the nonlinear problem. In the algorithm three programs are called `CMD` which performs computation of the mesh dynamics, `CSD` which performs the computation for the structure dynamics and `CFD` which performs the computation for the fluid dynamics. The structure of the scheme is given in algorithm in Table 1.

2.1. Notes on the FSI algorithm

Two codes (`CFD` and `CSD`) are running simultaneously. For simplicity, the basic algorithm can be thought as if there were no '*concurrence*' between the codes, i.e. at a given time only one of them is running. This can be controlled using '*semaphores*' and this is done using MPI '*synchronization messages*'.

The most external loop is over the time steps. In this work, both fluid and structure partitions are integrated with the trapezoidal rule (with trapezoidal parameter $0<\alpha_{\text{trap}}\leqslant 1$). Internal to the time step loop is the '*stage loop*'. '*Weak coupling*' is achieved if only one stage is performed (i.e. $n_{\text{stage}}=1$). In each stage the fluid is first advanced using the previously computed structure state $\mathbf{u}^n$ and the current estimate value $\mathbf{u}^{n+1,i}$. In this way, a new estimate for the fluid state $\mathbf{w}^{n+1,i+1}$ is computed. Next the structure is updated using the forces of the fluid

Table 1
Outline of FSI staged algorithm

1:	Initialize variables:
2:	**for** $n = 0$ to n_{step} **do** { *Main time step loop* }
3:	$t^n = n\Delta t$,
4:	{ *CFD CODE* : }
5:	$\mathbf{X}^n = \text{CMD}(\mathbf{u}^n)$ { *run CMD code* }
6:	$\mathbf{u}^{(n+1)P} = \mathbf{u}^{(n+1,0)} = \text{predictor}(\mathbf{u}^n, \mathbf{u}^{n-1})$ { *compute predictor* }
7:	$i = 0$, $n_{\text{stage}} = 0$
8:	**repeat** { (*stage loop*) }
9:	{ *CFD CODE* : }
10:	$\mathbf{X}^{n+1,i+1} = \text{CMD}(\mathbf{u}^{n+1,i})$
11:	{ *Compute skin normals and velocities* }
12:	**repeat** { *fluid Newton loop* }
13:	$\mathbf{w}^{n+1,i+1} = \text{CFD}(\mathbf{w}^n, \mathbf{X}^{n+1,i+1}, \mathbf{X}^n)$
14:	**until** *convergence* (*fluid Newton loop*)
15:	{ *CSD CODE* : }
16:	compute structural loads $(\mathbf{w}^n, \mathbf{w}^{n+1,i+1})$
17:	**repeat** { *structure Newton loop* }
18:	$\mathbf{u}^{n+1,i+1} = \text{CSD}(\mathbf{w}^n, \mathbf{w}^{n+1,i+1})$
19:	**until** *convergence* (*structure Newton loop*)
20:	$i = i + 1$, $n_{\text{stage}} = i$
21:	**until** *convergence* (*stage loop*)
22:	**end for**

from states $\mathbf{w}^n$ and $\mathbf{w}^{n+1,i+1}$. At the first stage, the state $\mathbf{u}^{n+1,0}$ is predicted using a second or higher order approximation (see Eq. (1)). Inside the *stage loop* there are Newton loops for each code to solve the nonlinearities. In this application the 'computational structure dynamics' is linear, so $n_{\text{nwt}} = 1$. The stage loop is iterated until convergence on both states is achieved.

Once the coordinates of the structure are known, the coordinates of the fluid mesh nodes are computed by a '*computational mesh dynamics*' code, which is symbolized as

$$\mathbf{X}^n = \text{CMD}(\mathbf{u}^n).$$

Even though this step may be performed with a general strategy using both nodal reallocation or remeshing, in this paper only the former is adopted, keeping the topology unchanged. Relocation of mesh nodes can be done using an elastic or pseudo-elastic model [14] through a separate PETSc-FEM parallel process (code named MESH-MOVE). For the simple geometry of the example in this paper a simple spine strategy is used.

The general form of the predictor for the structure state was taken from Ref. [2] and can be written as

$$\mathbf{u}^{(n+1)P} = \mathbf{u}^n + \alpha_0 \Delta t \dot{\mathbf{u}}^n + \alpha_1 \Delta t (\dot{\mathbf{u}}^n - \dot{\mathbf{u}}^{n-1}). \tag{1}$$

It is at least first-order accurate when no predictor is employed and it may be improved to second order using the above predictor with some values for α_0 and α_1 according to the problem at hand (see Section 3.3.2 for a discussion about this subject).

At the beginning of each fluid stage there is a computation of skin normals and velocities. This is necessary due to the time dependent slip boundary condition for the inviscid case implemented as a constraint (see Eq. (3)) or also in the case of using a non-slip boundary condition for the viscous case where the fluid interface has the velocity of the moving solid wall, i.e. $\mathbf{v}|_{\Gamma_g} = \hat{\mathbf{v}}|_{\Gamma_g} = \dot{\mathbf{u}}|_{\Gamma_g}$.

3. Description of test case

The flutter of a flat solid plate aligned with a gas flow at supersonic Mach numbers (see Fig. 1) is studied and the critical Mach number is computed. It must be stressed that in this work we deal with both physical and numerical instabilities. They are, in general, uncorrelated, i.e. a temporal integration scheme can be unstable for a configuration of physical parameters that is well outside the flutter region and *vice versa*. This test is

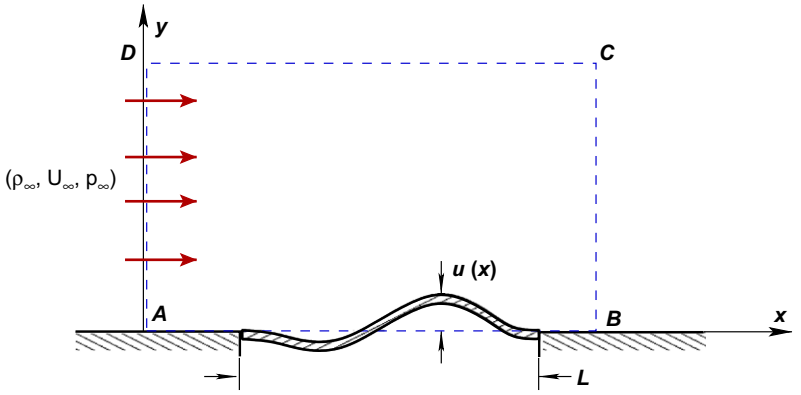

Fig. 1. Description of test.

relevant because the onset of physical instabilities is very sensitive to the precision in the transfer of forces and displacements. Afterwards (see Section 4) the stability of the numerical scheme will be assessed in a region far from the physically unstable region (flutter) in order to be sure that if any instabilities are detected, they come exclusively from the coupling process.

A uniform fluid at state $(\rho_\infty, U_\infty, p_\infty)$ flows over an horizontal rigid wall $y = 0$ parallel to it. This test case has been studied also in Ref. [2]. In a certain region of the wall $(0 \leqslant x \leqslant L)$ the wall deforms elastically following thin plate theory, i.e.

$$m\ddot{u} + D\frac{\partial^4 u}{\partial x^4} = -(p - p_\infty) + f(x,t), \tag{2}$$

where m is the mass of the plate per unit area in kg/m^2, $D = Et^3/12(1-\nu^2)$ the *bending rigidity* of the plate module in N m, E is the Young modulus in Pa, t the plate thickness in m, ν the Poisson modulus, u the normal deflection of the plate in m, defined on the region $0 \leqslant x \leqslant L$ and null outside this region, p the pressure exerted by the fluid on the plate in Pa, f is an external force in N and will be described later. The plate is clamped at both ends, i.e. $u = (\partial u/\partial x) = 0$ at $x = 0, L$. For the sake of simplicity the fluid occupying the region $y > 0$ is inviscid. The compressible Euler model with 'streamline upwind Petrov Galerkin' (SUPG) stabilization and 'anisotropic shock-capturing' method is considered [15]. A slip condition is assumed

$$(\mathbf{v} - \mathbf{v}_{\text{str}}) \cdot \hat{\mathbf{n}} = 0 \tag{3}$$

on the (curved) wall $y = u(x)$, where

$$\mathbf{v}_{\text{str}} = (0, \dot{u}),$$

$$\hat{\mathbf{n}} \propto \left(-\frac{\partial u}{\partial x}, 1\right) \tag{4}$$

are the velocity of the plate and its unit normal. Finally, initial conditions for both the fluid and the plate are taken as

$$u(x, t=0) = u_0(x),$$

$$\dot{u}(x, t=0) = \dot{u}_0(x),$$

$$(\rho, \mathbf{v}, p)_{\mathbf{X}, t=0} = (\rho, \mathbf{v}, p)_0 \quad \text{for } y \geqslant u_0(x). \tag{5}$$

Note that for the fluid pressure load on the plate the free stream fluid pressure is subtracted so that in the absence of any external perturbation ($f = 0$) the undisturbed flow $(\rho, \mathbf{v}, p)_{x,t} = (\rho, \mathbf{v}, p)_\infty$ is a solution of the problem for the initial conditions

$$u = 0,$$

$$\dot{u} = 0,$$

$$(\rho, \mathbf{v}, p)_{\mathbf{X},t=0} = (\rho, \mathbf{v}, p)_{\infty}. \tag{6}$$

3.1. Dimensionless parameters

As the fluid is inviscid, it is determined by the '*adiabatic index*' $\gamma = C_p/C_v = 1.4$ for air, and the Mach number $M_\infty = U_\infty/c_\infty$, where c_∞ is the speed of sound $c = \sqrt{\gamma p/\rho}$ for the undisturbed state.

Another dimensionless parameter can be built by taking the ratio between the characteristic time of the fluid which is $T_{\mathrm{fl}} = L/U_\infty$ and the characteristic time of the structure $T_{\mathrm{str}} = \sqrt{mL^4/D}$. For practical reasons we take the square of this ratio

$$N_T = \left(\frac{T_{\mathrm{fl}}}{T_{\mathrm{str}}}\right)^2 = \frac{D}{mL^2U_\infty^2}. \tag{7}$$

Finally, a (dimensionless) number can be formed by taking the ratio between the mass of the fluid being displaced by the structure and the structure mass

$$N_M = \frac{\rho_\infty L^3}{mL^2} = \frac{\rho_\infty L}{m}. \tag{8}$$

The same parameters as reported in Ref. [2] are considered. In this contribution, flutter was studied near the point $M_\infty = 2.27$, $N_T = 4.3438 \times 10^{-5}$ and $N_M = 0.054667$. The flutter region was studied by varying the M_∞ value while keeping ρ_∞ and the structure parameters (m, L, D) constant (so that N_M constant and $N_T \propto M_\infty^{-2}$), and the same approach is taken here. The dimensionless parameters are obtained by choosing the following dimensional values:

$$\rho_\infty = 1\,\mathrm{kg/m^3},$$

$$p_\infty = 1/\gamma = 0.71429\,\mathrm{Pa},$$

$$U_\infty = M_\infty \quad (\text{since } c_\infty = \sqrt{\gamma p_\infty/\rho_\infty} = 1\,\mathrm{m/s}),$$

$$D = 0.031611\,\mathrm{N\,m},$$

$$m = 36.585\,\mathrm{kg/m^2},$$

$$L = 2\,\mathrm{m}. \tag{9}$$

3.2. Houbolt's model

In this section the linear flutter instability by means of the modal analysis is studied. First, the '*Houbolt approximation*' [16] is assumed for the fluid,

$$p - p_\infty = C_x\frac{\partial u}{\partial x} + C_t\frac{\partial u}{\partial t},$$

$$C_x = \frac{\rho_\infty U_\infty^2}{\sqrt{M_\infty^2 - 1}},$$

$$C_t = \frac{\rho_\infty U_\infty (M_\infty^2 - 2)}{(M_\infty^2 - 1)^{3/2}}. \tag{10}$$

With this approximation the governing equation for plate deflection (Eq. (2)) becomes

$$m\ddot{u} + D\frac{\partial^4 u}{\partial x^4} = -C_x\frac{\partial u}{\partial x} - C_t\frac{\partial u}{\partial t}. \tag{11}$$

3.2.1. Galerkin model for the finite length plate

The plate normal displacement is expanded in a global basis using

$$u(x) = \sum_{k=1}^{N} a_k \psi_k(x),$$

$$\psi_k(x) = \frac{4x(L-x)}{L^2}\sin(k\pi x/L). \tag{12}$$

These basis functions satisfy the essential boundary conditions for the plate equation $u = (\partial u/\partial x) = 0$ at $x = 0, L$. Replacing the Houbolt approximation in Eq. (2), using Galerkin method and integrating by parts as needed, the following matrix equation is obtained:

$$\mathbf{M}\ddot{\mathbf{a}} + \mathbf{K}\mathbf{a} + \mathbf{H}_x\mathbf{a} + \mathbf{H}_t\dot{\mathbf{a}} = 0, \tag{13}$$

where

$$M_{jk} = \int_0^L m\psi_j(x)\psi_k(x)\,\mathrm{d}x,$$

$$K_{jk} = \int_0^L D\psi_j''(x)\psi_k''(x)\,\mathrm{d}x,$$

$$H_{x,jk} = \int_0^L C_x\psi_j(x)\psi_k'(x)\,\mathrm{d}x,$$

$$H_{t,jk} = \int_0^L C_t\psi_j(x)\psi_k(x)\,\mathrm{d}x. \tag{14}$$

Solution of these system of ODEs can be found by standard operational methods by replacing $\mathbf{a}(t)$ by the *ansatz*

$$\mathbf{a}(t) = \hat{\mathbf{a}}\mathrm{e}^{\lambda t} \tag{15}$$

leading to the eigenvalue equation

$$(\lambda^2\mathbf{M} + \lambda\mathbf{H}_t + \mathbf{K} + \mathbf{H}_x)\hat{\mathbf{a}} = 0. \tag{16}$$

Flutter is detected whenever some eigenvalue λ has a positive real part.

3.2.2. Numerical solution details

In order to determine the critical Mach number M_{cr}, the interval $1.8 \leqslant M \leqslant 3.0$ was swept with an increment of 0.01.

Regarding the convergence of series in Eq. (12), the critical Mach number M_{cr} remains constant within a tolerance of 10^{-5} for $N \geqslant 10$.

The quadratic eigenvalue problem of size N is solved by converting it to a linear eigenvalue problem of size $2N$ (and then finding eigenvalues and eigenvectors).

3.2.3. Results

Using for instance the values described in Eq. (9) with $N = 20$ terms in the series, and varying Mach from 1.8 to 3 the results shown in Fig. 2 are obtained. For $M_\infty < M_{\mathrm{cr}} = 2.265$, all the eigenvalues have negative real

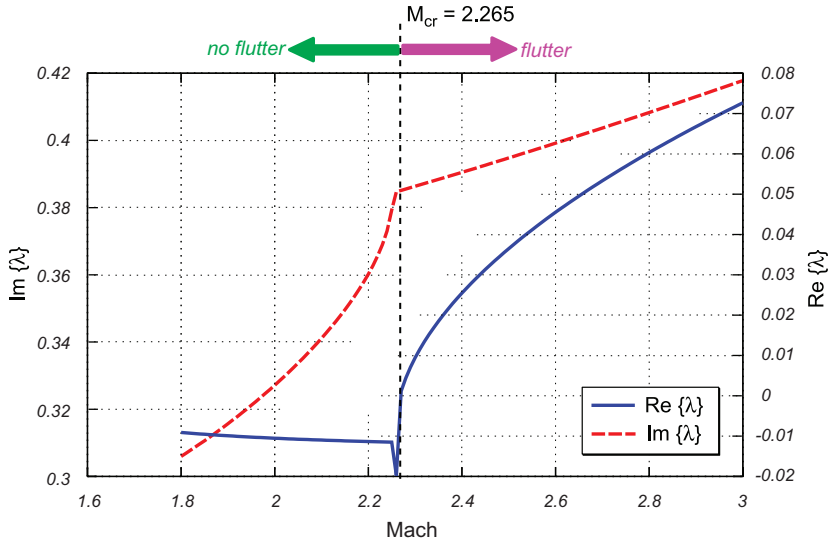

Fig. 2. Lowest frequency mode for test case.

part being stable. For $M_\infty > M_{cr} = 2.265$ there are two complex conjugate roots with positive real part. In Fig. 2 the real and imaginary part of the unstable mode are plotted. For $M_\infty < M_{cr} = 2.265$ the eigenvalue with the lower frequency was taken as a continuation of the flutter mode. It was checked that for $M_\infty < M_{cr} = 2.265$ the plate does positive power on the fluid, whereas for $M_\infty > M_{cr} = 2.265$ the converse is true. The instantaneous power done by the plate on the fluid is

$$P = \int_{x=0}^{L} p\dot{u}\,\mathrm{d}x. \tag{17}$$

3.2.4. Flutter region

A large number of flutter computations in the space N_M, N_T, M_∞ were performed in order to determine the flutter region. A grid of 20×20 points in the region $[0.001 \leqslant N_M \leqslant 0.1] \times [10^{-5} \leqslant N_T M_\infty^2 \leqslant 10^{-3}]$ was scanned. For each point in the grid instability is scanned in the Mach region $1.8 \leqslant M_\infty \leqslant 3$. The flutter region has the following form:

$$\frac{N_M}{N_T M_\infty^2} < 200 \text{ no flutter for any Mach number,}$$

$$\frac{N_M}{N_T M_\infty^2} > 300 \text{ flutter for the lowest Mach number considered } (M_\infty \geqslant 1.8). \tag{18}$$

In the intermediate region flutter is produced. This suggests that flutter is highly correlated to quantity

$$\frac{N_M}{N_T M_\infty^2} = \frac{\rho_\infty L^3 c_\infty^2}{D} \tag{19}$$

which happens to be independent of the density of the plate.

A simple model presented in Ref. [4] draws a similar conclusion. The explanation is as follows. In that reference, the term proportional to $(\partial u/\partial t)$ is neglected. This is true if the characteristic times of the structure are much lower than those of the fluid, i.e. $N_T \ll 1$. This is a valid assumption because of all points in the grid located in the region $N_T < 10^{-3}$ are considered. But if the temporal term in the Houbolt approximation is neglected the characteristic equation can be written in the form

$$\det(\bar{\lambda}^2 \bar{\mathbf{M}} + \mathbf{K} + \mathbf{H}_x) = 0, \tag{20}$$

where

$$\bar{\lambda} = \sqrt{m}\lambda,$$

$$\bar{\mathbf{M}} = \frac{1}{\sqrt{m}}\mathbf{M}. \tag{21}$$

As now the coefficients in $\bar{\mathbf{M}}$, $\mathbf{K}$, $\mathbf{H}_x$ do not depend on m, neither do the eigenvalues of Eq. (20), and then by Eq. (21) the λ eigenvalues are of the form

$$\lambda_j = \frac{\bar{\lambda}_j}{\sqrt{m}}, \tag{22}$$

with $\bar{\lambda}$ not depending on m. This means that the sign of the real part of the λ is independent of m.

3.3. FSI code results

The aeroelastic problem defined above was modeled with the strongly coupled partitioned algorithm described in Section 2 with a mesh of 12 800 quadrilateral elements for the fluid and 5120 for the plate. As the flow is supersonic only a small entry section of $1/8L$ upstream the plate and $1/3L$ downstream is considered. The vertical size of the computational domain was chosen as $0.8L$. It is assured that no reflection from the upper boundary affects the plate itself when considering these sizes for the fluid domain.

3.3.1. Determination of flutter region

This section presents some results obtained with PETSc-FEM code using the weak coupling between fluid and structure, i.e. $n_{\text{stage}} = 1$. The physical characteristics of the plate are the same as in previous section. In order to find (numerically) the *critical Mach number* for this problem a sweep in the Mach number in the range of 1.8–3.2 was done. Results for some Mach numbers can be seen in Figs. 3–8. In these plots the time evolution of displacements of several points distributed along the skin plate are shown. The fluid density field and the structure displacement at Mach = 3.2 (flutter region) for a given time step is shown in Figs. 9 and 10.

For Mach numbers below the M_{cr}, Figs. 3–5, the maximum plate displacement grows until the forces exerted by the fluid dump the plate displacements. The damping rate (measured for instance as the time needed to reduce the amplitude by a given fixed factor, say 30%) grows with the Mach number. For Mach numbers

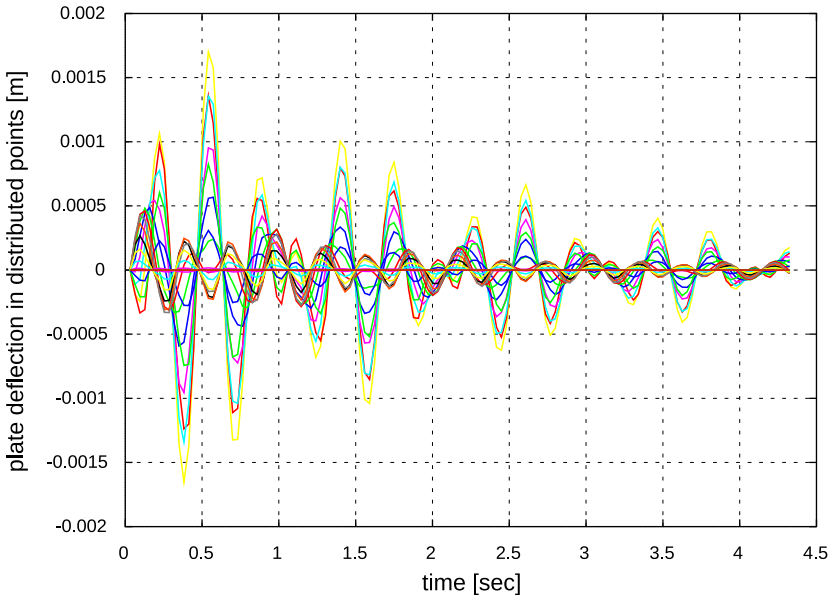

Fig. 3. Plate deflection in distributed points along plate at $M = 1.8$.

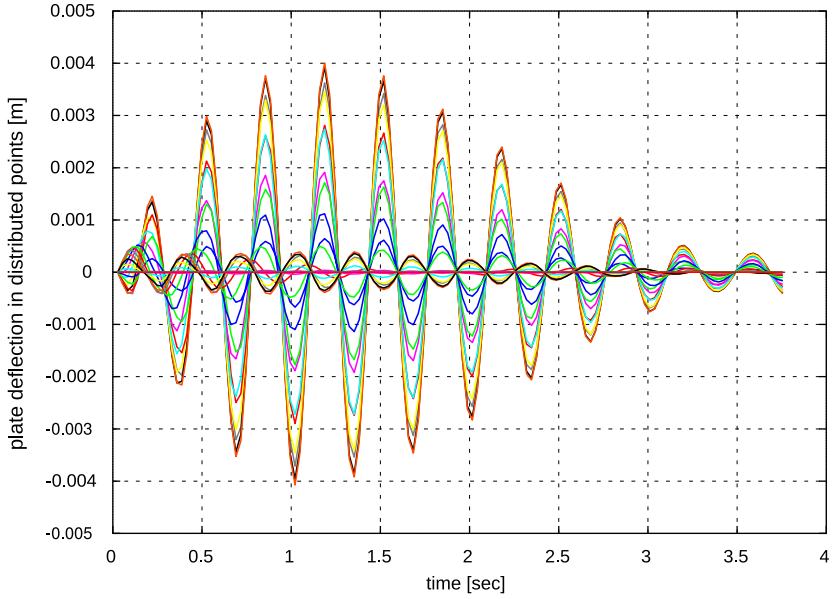

Fig. 4. Plate deflection in distributed points along plate at $M = 2.225$.

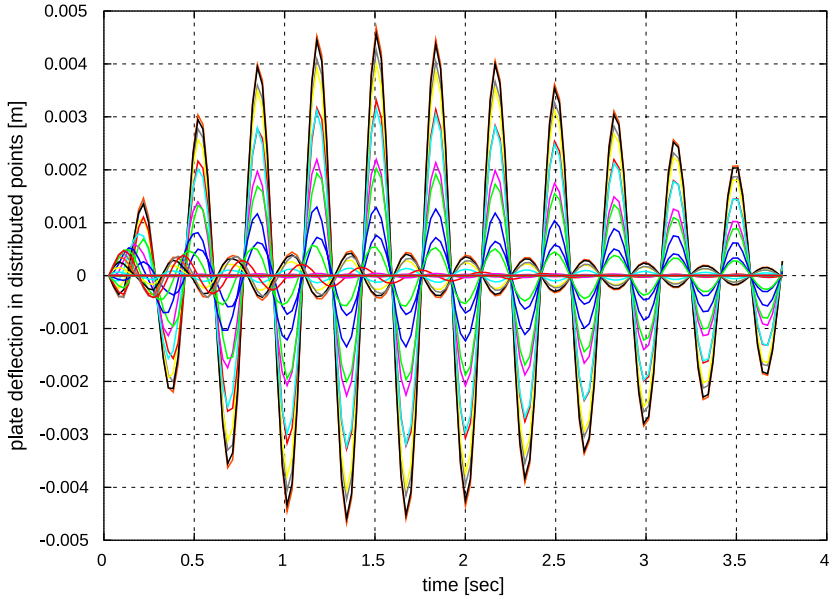

Fig. 5. Plate deflection in distributed points along plate at $M = 2.25$.

near the M_{cr}, Fig. 6, the maximum amplitude grows slightly. The flutter mode is triggered at this point. For Mach numbers above the M_{cr}, Figs. 7–10, the fluid forces cannot damp the structure response and displacements grow without limit in an unstable fashion according to the theory.

3.3.2. Time accuracy

If the stage loop converges, i.e. $(\mathbf{u},\mathbf{w})^{n+1,i} \rightarrow (\mathbf{u},\mathbf{w})^{n+1,*}$, then it can be shown that the limit states $(\mathbf{u},\mathbf{w})^{n+1,*}$ satisfy the fully implicit, strong coupled equations. The main effect of the staged algorithm is to have a strong coupling and then, enhanced stability, regardless the time accuracy. To understand how to specify the

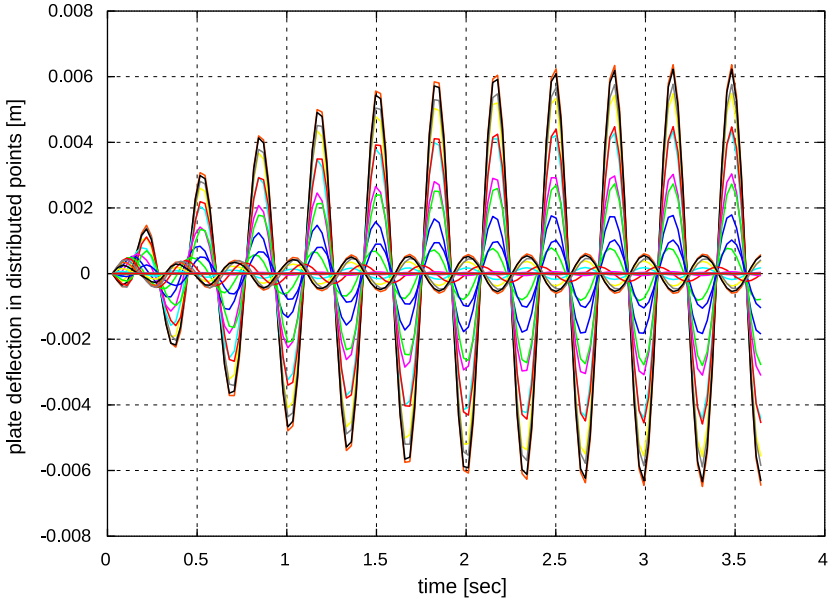

Fig. 6. Plate deflection in distributed points along plate at $M = 2.275$.

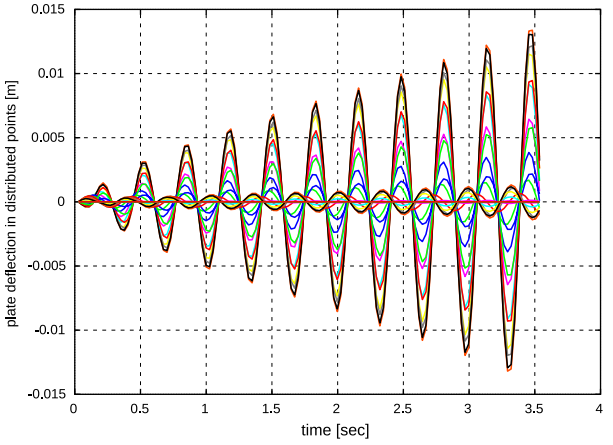

Fig. 7. Plate deflection in distributed points along plate at $M = 2.3$.

parameters in Eq. (1) for predictors a simple two dofs wake oscillator model represented by two second-order differential equations as follows:

$$m_z\ddot{z} + c_z\dot{z} + k_z z = f_z(\ddot{y}, \dot{y}, y, t),$$

$$m_y\ddot{y} + c_y\dot{y} + k_y y = f_y(\ddot{z}, \dot{z}, z, t), \tag{23}$$

with (m, c, k) the mass, the damping and the stiffness parameters for each degree of freedom. In this simple model, y, z represent the structure and fluid states in the CSD and CFD codes in algorithm in Table 1. The forcing terms at the right hand side contain the coupling between the two blocks. This coupling may be formulated in terms of the main variables and their two first derivatives, generally velocities and accelerations. If the coupling contains only the main variables, i.e. $f_z(y, t)$ and $f_y(z, t)$, the predictor with $\alpha_0 = 1$ and $\alpha_1 = 0$ achieves second-order accurate in time solutions. If the coupling contains velocities it is necessary to use $\alpha_1 = \frac{1}{2}$ to recover second order in time. In FSI problems solved via ALE it is known that the mesh velocity dependent

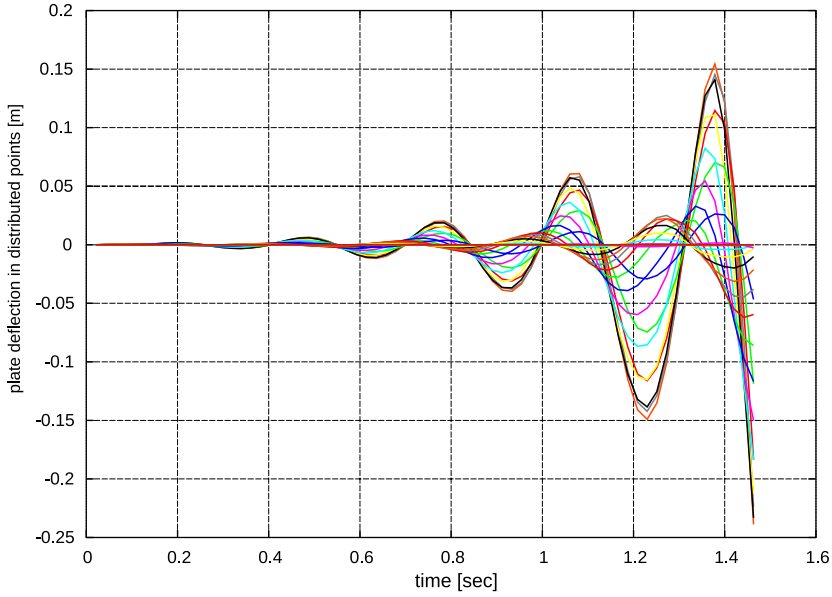

Fig. 8. Plate deflection in distributed points along plate at $M = 3.2$.

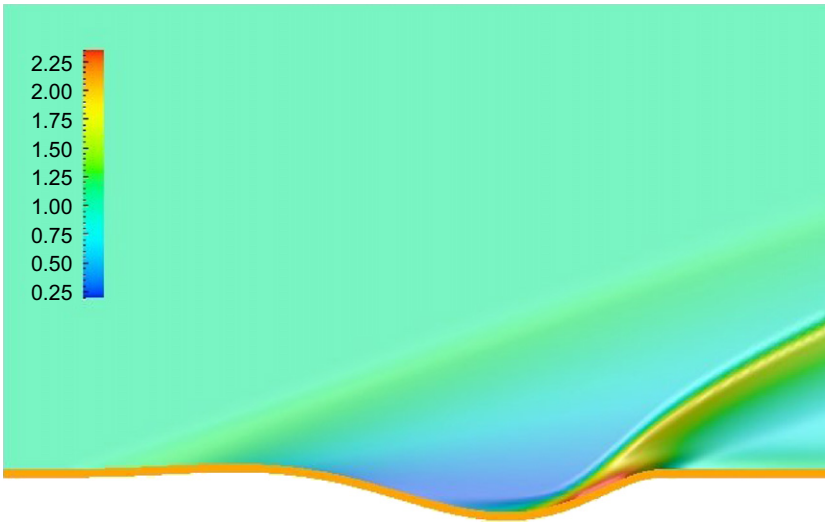

Fig. 9. Fluid and structure fields at $M = 3.2$. Colormap = fluid density, time = 1.46 s.

of the fluid–solid interface velocity is incorporated in the formulation, therefore to guarantee second order in time accuracy it is necessary to use $\alpha_0 = 1$ and $\alpha_1 = \frac{1}{2}$ for the predictor.

Note that, if the Crank–Nicolson scheme is used for the time integration of both the structure and the fluid equations and the predictor is chosen with at least second-order precision, then the whole algorithm is second order, *even if only one stage is performed* see Ref. [17].

In Fig. 11 the error obtained after the simulation of a certain fixed amount of time t_0 and increasing time refinement is shown. The exact solution is estimated through a Richardson extrapolation with the two more refined simulations for the more accurate scheme ($\alpha_{\text{trap}} = 0.5$). The error at t_0 is evaluated for a certain number of different Δt values. It is verified that for $\alpha_{\text{trap}} = 0.6$ the scheme is first-order accurate, whereas for $\alpha_{\text{trap}} = 0.5$ precision is $O(\Delta t^2)$. When using $\alpha_{\text{trap}} = 0.5$ with no predictor (Eq. (1)), a second-order convergence is still obtained.

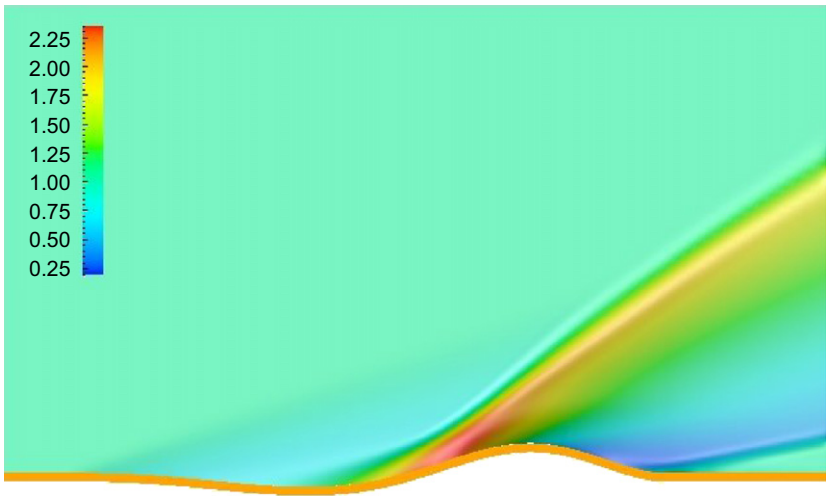

Fig. 10. Fluid and structure fields at $M = 3.2$. Colormap = fluid density, time = 1.68 s.

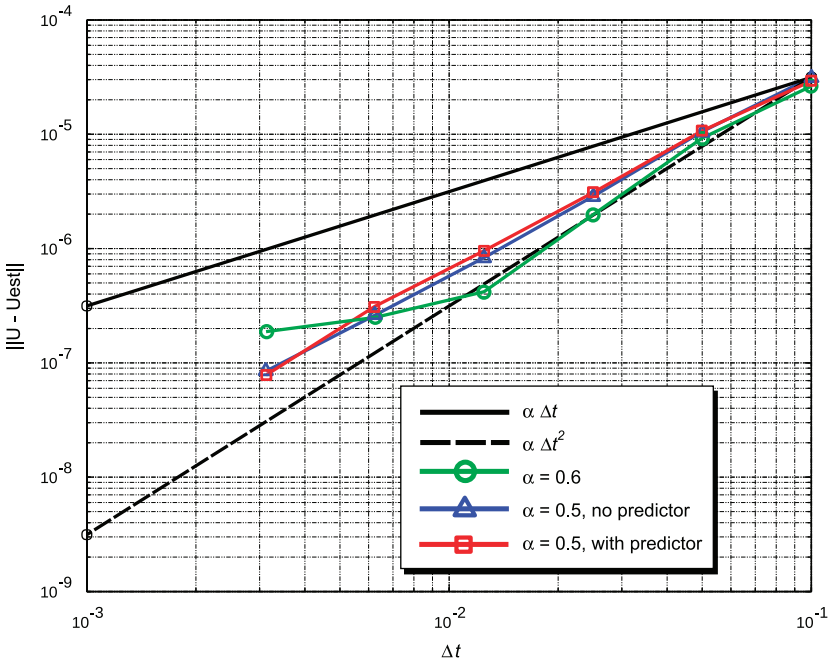

Fig. 11. Experimentally determined order of convergence with Δt for the uncoupled algorithm with fourth-order predictor.

3.3.3. *Convergence of stage loop*

The convergence of the stage loops has been assessed by running the test case over 20 time steps and performing 10 stages at each time step. In Fig. 12 the convergence of the fluid state (i.e. $\|\mathbf{u}^{n+1,i+1} - \mathbf{u}^{n+1,i}\|$) for all the time steps (convergence curves of the time steps are concatenated) is shown. Analogously, the convergence of the structure is plotted in Fig. 13. The average convergence is one order of magnitude per stage or higher, suggesting that for such a situation a small n_{stage} (2 or 3) would be enough.

3.3.4. *Stability of the staged algorithm*

The following numerical test allows to evaluate the stability of the staged algorithm presented in Section 2. The example is similar to the aeroelastic test case presented in Section 3 with some different parameters for the plate in order to produce larger plate deformations and stronger physical instabilities. Some parameters are

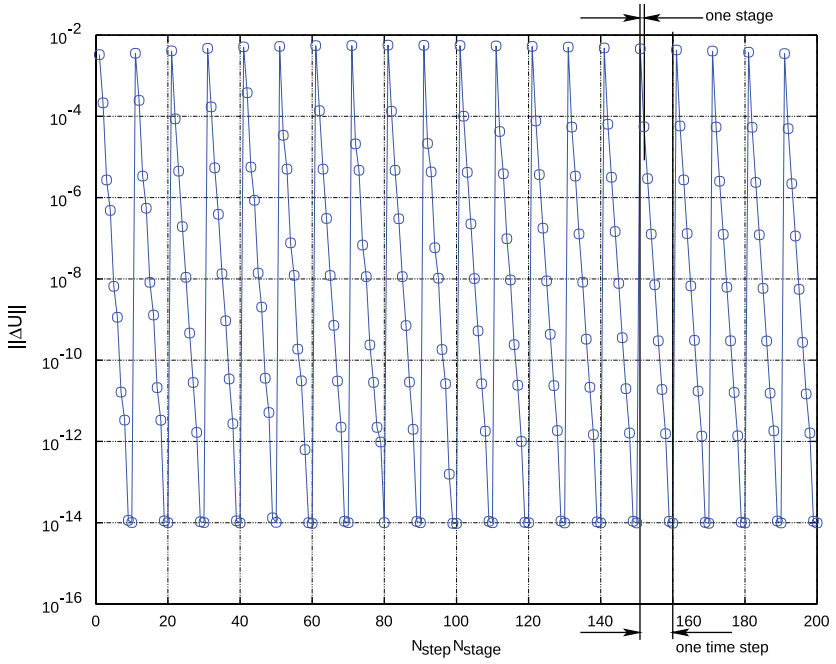

Fig. 12. Convergence of fluid state in stage loop.

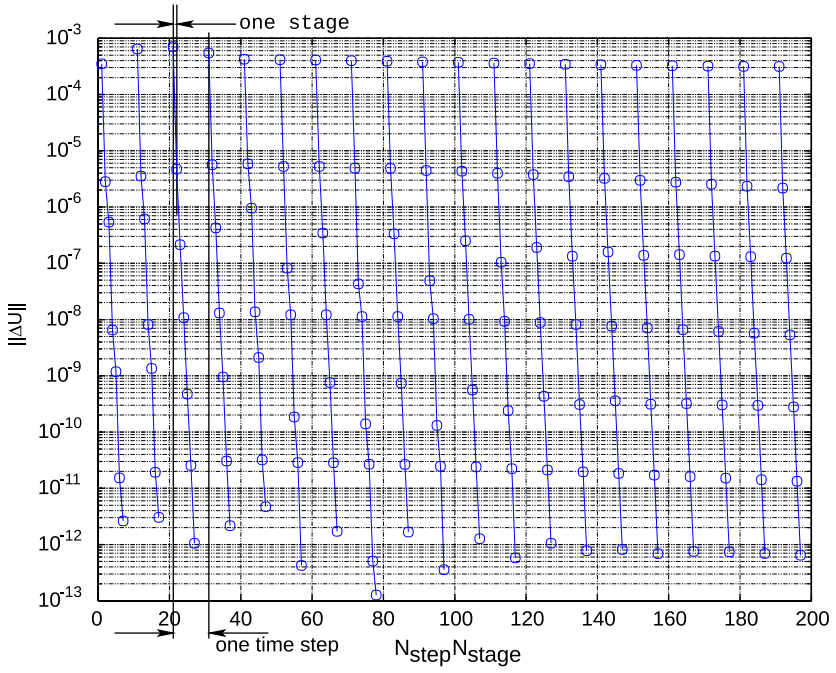

Fig. 13. Convergence of structure state in stage loop.

similar to those presented in Eq. (9). Here, only the parameters that have been modified and the dimensionless parameters that may be obtained with them are included.

$$U_\infty = M_\infty = 2,$$

$$t = 0.06,$$

$$v = 0.33,$$

$$m = 0.002,$$

$$E = 39.6,$$

$$D = 8.0 \times 10^{-4},$$

$$N_T = \frac{D}{mL^2 U_\infty^2} = 0.025,$$

$$N_M = \frac{\rho_\infty L}{m} = 1000.0. \tag{24}$$

Therefore according to Section 3.2.4

$$\frac{N_M}{N_T M_\infty^2} = 10\,000 > 300 \tag{25}$$

implies that the flow is inside the flutter region.

The following figures show results obtained with both strategies, the staged and non-staged algorithms.

The vertical displacements on some points of the plate for the staged algorithm using $n_{\text{stage}} = 5$ after approximately 1300 time steps are shown in Fig. 14. The results for the non-staged algorithm diverge at 40 time steps and are shown in Fig. 15. The time step chosen for the non-staged algorithm was one-fifth of the time step used with the staged one (i.e. $\Delta t_{\text{non-staged}} = \Delta t_{\text{staged}}/n_{\text{stage}}$). In this way the comparison of the stability of the two strategies is performed *at the same computational cost* (assuming that the computational cost of a *stage* in the *staged* algorithm is similar to the cost of a *time step* in the *non-staged* one).

Even though the staged algorithmic shows an extra stability compared with the non-staged one, the conclusions about this numerical experiment are not obvious because the flow regime is in a flutter condition.

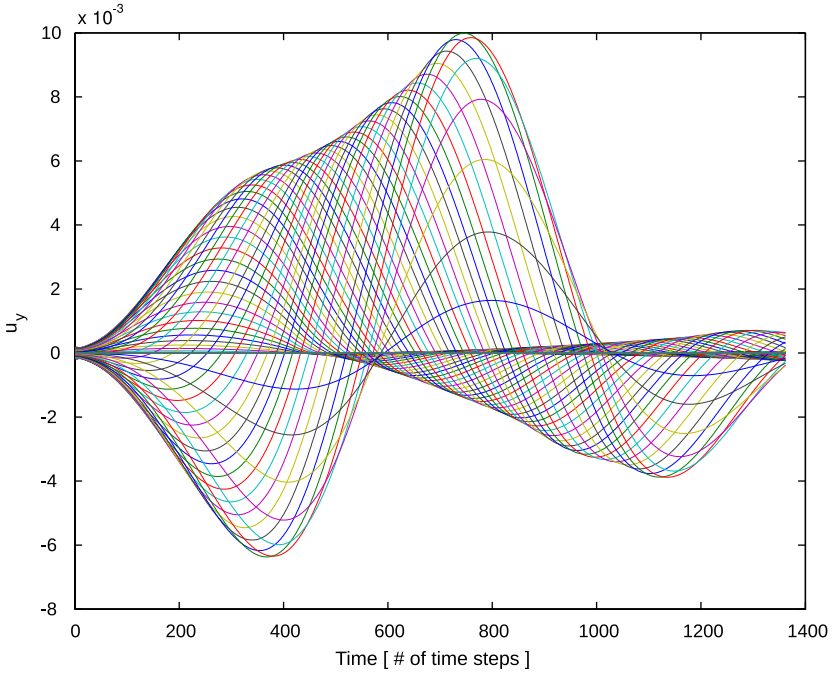

Fig. 14. Stability analysis—staged algorithm with $n_{\text{stage}} = 5$. Vertical displacements of the plate vs. time.

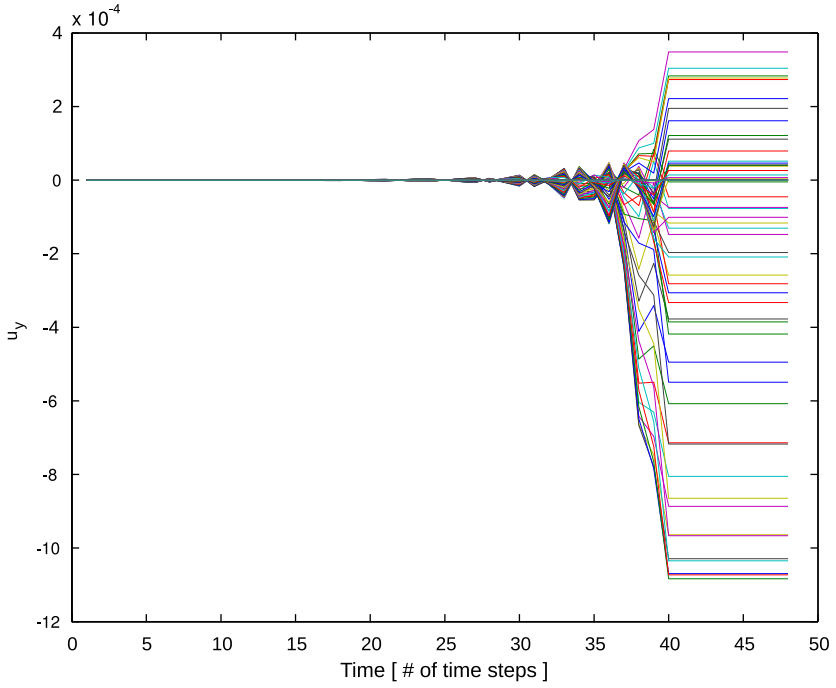

Fig. 15. Stability analysis—non-staged algorithm. Vertical displacements of the plate vs. time.

Further work needs to be done towards the understanding about how the staged algorithmic improves the stability of the whole coupled problem.

4. Stability of the weak/strong staged coupling outside the flutter region

This section describes the stability properties of the weak coupling when the free stream conditions and plate parameters are such that the oscillations due to flutter do not appear. The flutter region can be characterized by the dimensionless number $\mathrm{FL} = N_M/N_T M_\infty^2$ (see the previous section). Therefore, in order to study the stability behavior of the weak/strong algorithms ($n_{\mathrm{stage}} = 1$ and $n_{\mathrm{stage}} > 1$, respectively) intrinsic to the physical coupling, the region $\mathrm{FL} \ll 200$ is studied, particularly $\mathrm{FL} = 12$ is chosen. This non-dimensional number does not depend on plate density m. Then m can be varied in a wide range, seeking for instabilities of the numerical integration scheme, avoiding the flutter region. The idea is to find a value for m for which the weak coupling algorithm becomes unstable while the strong coupling and the uncoupled subproblems (fluid and structure) remain stable. The tolerance for convergence of the non-linear loop (Newton iteration) was 10^{-5}. The mesh is the same as in the previous simulations and the Courant number is $\mathrm{CFL} = 0.5$. The plate mass density varies in the range $m = 35$ and 0.0001. It was found that the critical value is $m = 0.65$. The weak coupling scheme is stable above this critical value, while instabilities are observed below it. Instabilities disappear when the strong coupling scheme with $n_{\mathrm{stage}} = 2$ is considered (see Figs. 16 and 17). Moreover, even when a lower value of m is used, for instance $m = 0.0135$ and $\mathrm{CFL} = 1$, only two stages are enough to achieve convergence of the strong coupling algorithm. In the case of $m = 0.0001$ a smaller CFL number is needed (e.g. $\mathrm{CFL} = 0.5$) in order to have at least 15 time steps in one period (recall that the plate frequency depends on plate density). In all cases, it was checked that each of the separated subsystems (fluid and structure) are stable i.e. the instabilities are exclusively attributed to the weak coupling.

Even though the convergence of the coupled problem is not affected when considering a very small plate density and a strong partitioned scheme, it is necessary to refine the fluid mesh in the normal direction to the plate in order to have a better definition of the problem in that direction, i.e. a wave train is propagated in the fluid with the plate frequency (recall that the plate frequency grows as the plate density decrease,

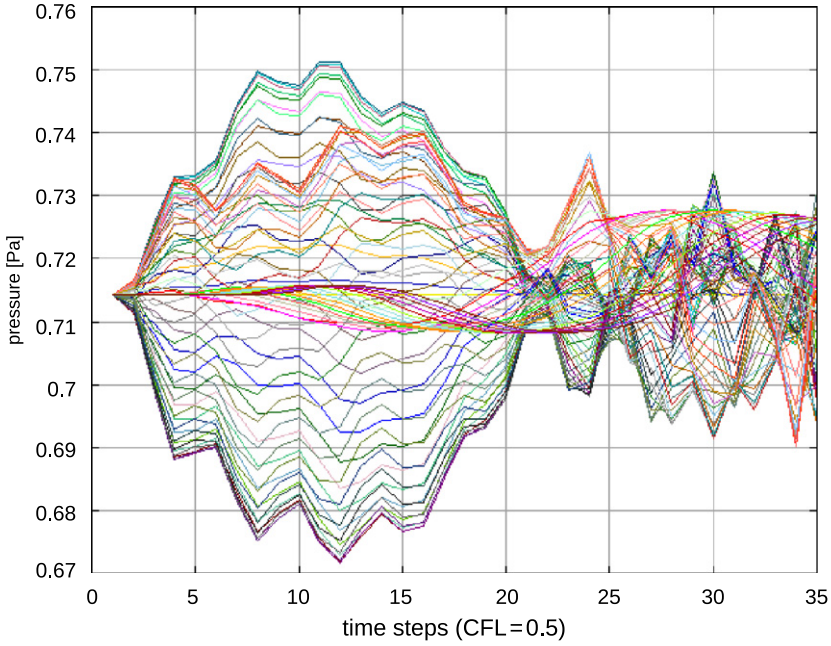

Fig. 16. Unstable weak coupling for $m = 0.0135$ and CFL $= 0.5$.

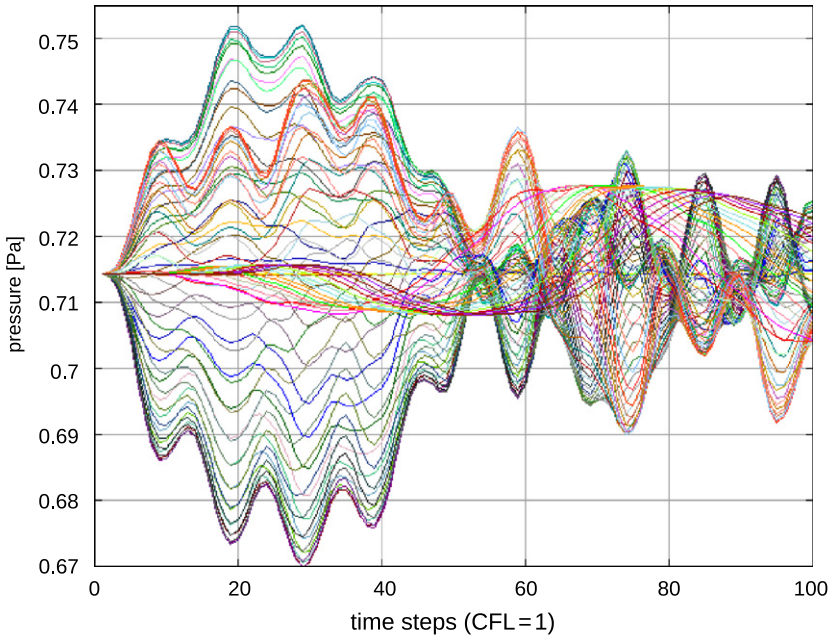

Fig. 17. Stable staged coupling for $m = 0.0135$, CFL $= 1$ and $n_{\text{stage}} = 2$.

$\omega_{\text{str}} = 2\pi/T_{\text{str}} = [mL^4/D]^{-1/2}$). In the coupled simulation the interaction may produce the amplification of the pressure and plate displacements. This fact can be shown in Figs. 18 and 19. Fig. 18 shows the plate deflection when $m = 0.00135$ and mesh size of the fluid mesh near the plate is $h_y = 0.018808\,\text{m}$ and

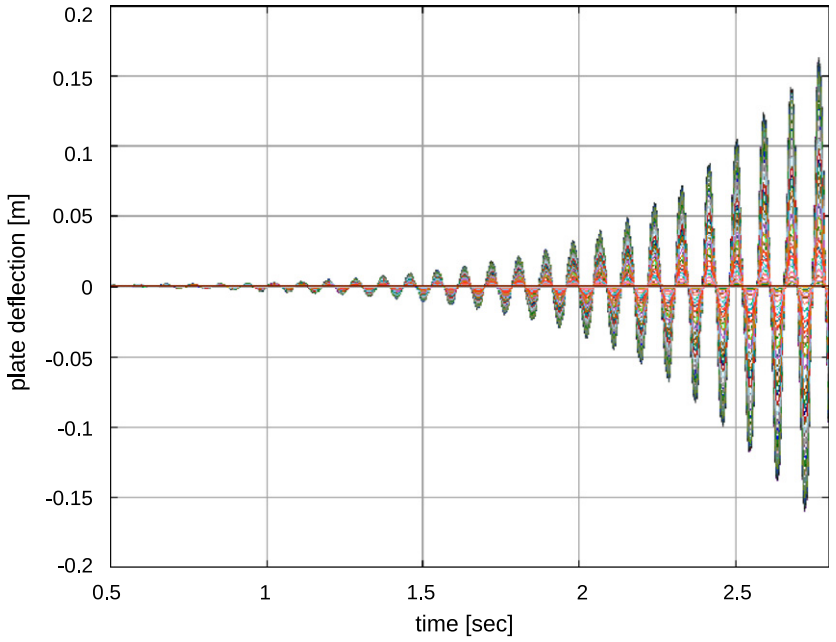

Fig. 18. Strong partitioned scheme in a coarse mesh.

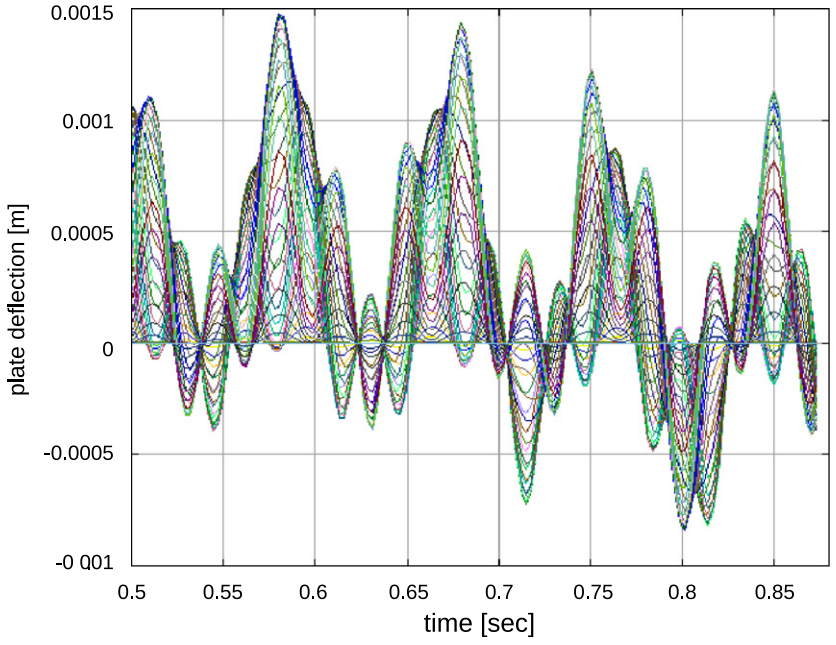

Fig. 19. Strong partitioned scheme in a fine mesh.

$h_x = 0.035625$ m. Fig. 19 shows the same results when considering an homogeneous refinement (i.e. $h_y = 0.00932$ m and $h_x = 0.01781$ m). The coarse mesh exhibit a spurious vibration mode similar to a flutter mode that is corrected in the finer mesh.

Other researchers [11,12] have focused on the stability of the weak coupling algorithm for incompressible flows. They rely on simplified models based on potential or very low Reynolds approximations and give

estimates for the conditional stability of the weak coupled algorithm in terms of the physical parameters and mesh sizes (structure and fluid). In this context, the aim of the present work is to shed some light on the stability of the weak coupling strategy for more complex flow, namely the compressible supersonic regime.

5. Conclusions

Stability is enhanced through a strong coupling scheme and it shows to be necessary for situations where the structural response is fast. Partitioned schemes using staged strong coupling shows to be very efficient avoiding the tedious and problem dependent task of building a monolithic coupling formulation. For the benchmark considered in this work two stages were enough for having the same behavior of the monolithic scheme. Furthermore, the staged strategy provides a smooth blending between weak coupling and strong coupling, i.e. moderately coupled problems that cannot be treated with the pure weak coupling approach, can be solved with the staged algorithm using few stages per time step.

Time-accuracy shows to be in agreement with the accuracy of the underlying fluid and structure solvers, if an accurate enough predictor is used. Second-order accuracy can be obtained with second-order fluid and structure solvers, and one stage coupling with a high order predictor, as already reported in Ref. [2].

The elastic flat plate problem is geometrically simple, but gives physical insight in the flutter phenomena, and was very useful in testing the proposed algorithm in a wide range of non-dimensional parameters.

Acknowledgments

This work has received financial support from Consejo Nacional de Investigaciones Científicas y Técnicas (CONICET, Argentina, Grant PIP-5271/2005), Universidad Nacional del Litoral (Argentina, Grant CAI + D 2005-10-64) and ANPCyT (Argentina, Grants PICT 12-14573/2003 and PME 209/2003). Extensive use of freely distributed software such as *GNU/Linux* OS, MPICH, PETSc, Metis, Octave, OpenDX and many others is done in this work.

References

[1] V. Gnesin, R. Rzadkowski, A coupled fluid structure analysis for 3-d inviscid flutter of IV standard configuration, *Journal of Sound and Vibration* 49 (2005) 349–369.

[2] R. Piperno, C. Farhat, Partitioned procedures for the transient solution of coupled aeroelastic problems. Part II: energy transfer analysis and three-dimensional applications, *Computer Methods in Applied Mechanics and Engineering* 190 (2001) 3147–3170.

[3] E. Lefrancois, Numerical validation of a stability model for a flexible over-expanded rocket nozzle, *International Journal for Numerical Methods in Fluids* 49 (2005) 349–369.

[4] E. Dowell, E. Crawley, H. Curtiss, D. Peters, R. Scanlan, F. Sisto, *A Modern Course in Aeroelasticity*, Kluwer Academic Publishers, Dordrecht, 1995.

[5] J. Mouro, P. Le Tallec, Fluid structure interaction with large structural displacements, *Computer Methods in Applied Mechanics and Engineering* 190 (2001) 3039–3067.

[6] R. Codina, M. Cervera, Block-iterative algorithms for nonlinear coupled problems, in: M. Papadrakakis, G. Bugeda (Eds.), *Advanced Computational Methods in Structural mechanics*, CIMNE, Barcelona, 1995, pp. 115–134.

[7] S. Artlich, W. Mackens, Newton-coupling of fixed point iterations, in: W. Hackbusch, G. Wittum (Eds.), *Numerical Treatment of Coupled Systems*, Vieweg, Braunschweig, 1995.

[8] C.A. Felippa, K.C. Park, C. Farhat, Partitioned analysis of coupled mechanical systems, *Computer Methods in Applied Mechanics and Engineering* 190 (2001) 3247–3270.

[9] K.C. Park, C.A. Felippa, A variational principle for the formulation of partitioned structural systems, *International Journal for Numerical Methods in Engineering* 47 (2000) 395–418.

[10] W. Dettmer, D. Peric, A computational framework for fluid-rigid body interaction: finite element formulation and applications, *Computer Methods in Applied Mechanics and Engineering* 195 (2006) 1633–1666.

[11] P. Causin, J.F. Gerbeau, F. Nobile, Added-mass effect in the design of partitioned algorithms for fluid–structure problems, *Computer Methods Applied Mechanics and Engineering* 194 (2005) 4506–4527.

[12] M.A. Fernandez, J.F. Gerbeau, C. Grandmont, A projection semi-implicit scheme for the coupling of an elastic structure with an incompressible fluid, *International Journal for Numerical Methods in Engineering* 69 (2007) 794–821.

[13] M.A. Storti, N.M. Nigro, R.R. Paz, L.D. Dalcín, E.J. López, PETSc-FEM a general purpose, parallel, multi-physics FEM program ⟨www.cimec.org.ar/petscfem⟩.

[14] E.J. Lopez, N.M. Nigro, M.A. Storti, J. Toth, A minimal element distortion strategy for computational mesh dynamics, *International Journal for Numerical Methods in Engineering* 69 (9) (2006) 1898–1929.
[15] T. Tezduyar, M. Senga, Determination of the shock-capturing parameters in SUPG formulation of compressible flows, *Computational Mechanics WCCM IV*, Beijing, China, Tsinghua University Press, Springer, Berlin, 2004.
[16] J.C. Houbolt, A study of several aerothermoelastic problems of aircraft structures, Mitteilung aus dem Institut fur Flugzeugstatik und Leichtbau 5, E.T.H., Zurich, Switzerland, 1958.
[17] C. Farhat, K.G. van der Zee, P. Geuzaine, Provably second-order time-accurate loosely-coupled solution algorithms for transient nonlinear computational aeroelasticity, *Computer Methods in Applied Mechanics and Engineering* 195 (2006) 1973–2001.